

ARTICLE

Implementation of high-performance, freestanding flexible film masks through photosensitive polyimide for arbitrary surface micropatterns creation

Xuan Dong¹ | Siew Yin Chan² | Ruoqing Zhao¹ | Lei Luo¹ | Manzhang Xu^{1,3,4} | Jiuwei Gao¹ | Xin Ju² | Jing Wu² | Dongzhi Chi² | Xian Jun Loh² | Xuewen Wang^{1,3,4,5} 

¹Frontiers Science Center for Flexible Electronics (FSCFE) & Institute of Flexible Electronics (IFE), Northwestern Polytechnical University, Xi'an, China

²Institute of Materials Research and Engineering (IMRE), Agency for Science, Technology and Research (A*STAR), Innovis, Singapore, Singapore

³MIIT Key Laboratory of Flexible Electronics (KLoFE), Northwestern Polytechnical University, Xi'an, China

⁴Shaanxi Key Laboratory of Flexible Electronics (KLoFE), Northwestern Polytechnical University, Xi'an, China

⁵Key Laboratory of Flexible Electronics of Zhejiang Province, Ningbo Institute of Northwestern Polytechnical University, Ningbo, China

Correspondence

Xuewen Wang.

Email: iamxwwang@nwpu.edu.cn

Funding information

National Natural Science Foundation of China, Grant/Award Numbers: 62288102, 62304182, 62371397; Natural Science Foundation of Shaanxi Province, Grant/Award Numbers: 2022JQ-659, 2023-JC-YB-495; Fundamental Research Funds for the Central Universities, Grant/Award Number: 23GH02028

Abstract

Given the widespread presence of intricate surfaces, the development of electronics has generated a significant demand for surface patterning techniques capable of creating refined or novel patterns. Nevertheless, present surface patterning techniques suffer from complex processes, limited resolution, stringent conditions, and high manufacturing costs. Herein, we present a novel approach for arbitrary surface micropatterning using photosensitive polyimide (PSPI), enabling the in situ fabrication of electrodes without the need for a pattern-transferring process. On this basis, we have implemented a high-performance, freestanding flexible thin-film mask with high optical transparency that facilitates precise alignment of microelectrode patterns with the target material. It also exhibits exceptional mechanical properties suitable for long-term use and high-temperature applications, with a notable glass transition temperature of up to 300°C. The fabricated masks with thicknesses of 5–20 μm are well-suited for high-resolution applications, including those requiring sub-5 μm resolution. Furthermore, the creation of microelectrodes on a variety of surfaces utilizing the fabricated PSPI masks was successfully demonstrated. Our facile method provides a solid foundation for achieving efficient micropatterning for the fabrication of high-performance flexible electronics on complex surfaces.

This is an open access article under the terms of the [Creative Commons Attribution](https://creativecommons.org/licenses/by/4.0/) License, which permits use, distribution and reproduction in any medium, provided the original work is properly cited.

© 2024 The Author(s). FlexMat published by John Wiley & Sons Australia, Ltd on behalf of Nanjing University of Posts & Telecommunications.

KEYWORDS

flexible electronics, freestanding flexible film, micropatterning, photosensitive polyimide, shadow masks

1 | INTRODUCTION

The precise fabrication of structures with well-defined features at both the micro- and nano-scale is of utmost importance for the advancement of electronic devices.¹ In this context, surface micropatterning technologies play a pivotal role in enabling electronic devices with improved or novel functionalities.² Conventional photolithography techniques typically involve spinning photoresist on a planar or rigid substrate (e.g., Silicon wafer), followed by patterning using laser writing or electron beam lithography. Although photolithography is widely employed in microelectronics, its resolution and capability to construct patterns on non-planar and arbitrary surfaces still present many challenges. In nonplanar micropatterning, a pattern transfer process from the original to the target non-planar surface is necessary, which often introduces mechanical damage to the pattern.² In addition, photolithography requires the use of chemical solvents. These solvents are often incompatible with the organic materials in the subsequent process. Currently, techniques for patterning micro- and nanostructures on unconventional substrates are rapidly developing for applications in wearable electronics^{3–5} and implantable medical devices.^{6–8} Although methods have been developed that allow direct pattern formation, including transfer printing,⁹ ink-jet printing,¹⁰ 3D printing,¹¹ dynamic electrostatic lithography,¹² soft lithography,¹³ and microcontact printing,¹⁴ these methods still face the disadvantages of low resolution, high processing costs, and low applicability. Thus, it has become imperative to develop a versatile micro-patterning fabrication technique to combine the capability of creating patterns on nonplanar and arbitrary surfaces with high resolution to drive the miniaturization of electronic applications.¹⁵

Shadow mask is of great interest as an alternative micropatterning technique due to its simplicity of preparation process, good compatibility with a wide range of materials, and high adaptability to morphology.¹⁶ They can be generally classified as rigid masks or flexible masks. Rigid shadow masks are usually made of metals,¹⁷ metallic alloys,¹⁸ stainless steel,¹⁹ ceramic foils such as silicon (Si),²⁰ silicon carbide,²¹ silicon nitride,²² or a mixture of these materials. Due to their brittleness, rigid shadow masks are mainly used for micropatterning of planar surfaces. In sharp contrast, flexible shadow masks

are a key solution for achieving in situ non-planar patterning. It is generally made from elastomeric polymers and other polymer films. Among them, elastomeric polymer shadow masks mainly prepared from polydimethylsiloxane (PDMS),^{23–26} offer significant advantages in terms of optical transparency, biocompatibility, oxygen permeability, durability, and processing cost.²⁷ However, PDMS still has low resolution and poor mechanical properties, making it difficult to pattern on non-planar and arbitrary surfaces.²⁸ Besides, polymer thin-film shadow masks, such as dichloro-*2*-paracyclophane (parylene-C),^{29–31} polyimide,^{32,33} and photoresist materials,^{34–36} have recently attracted much attention for micropatterning due to their exceptional flexibility.³⁷ For example, parylene-C shadow masks require chemical vapor deposition (CVD), metal sputtering, photolithography, and etching in that order.³⁷ Polyimide shadow masks need to be etched with the help of photoresists, or patterned by laser ablation.³³ These processes are not only complex but also low-resolution and high-cost. Photoresist masks are usually used as a sacrificial layer or a non-freestanding structural layer, which also results in a complex manufacturing process.

Photosensitive polyimide (PSPI) is a polymer containing an imide and a photosensitive functional group. The photosensitive groups can undergo photochemical reactions in response to ultraviolet (UV) radiation. Based on the ease of photochemical reaction, PSPI can be directly patterned by photolithography without the need for a photoresist.³⁸ It is a flexible, lightweight, transparent, electric-insulating, and corrosion-resistant polymer. In particular, PSPI possesses superior mechanical properties³⁹ and high-temperature resistance⁴⁰ for a wide range of application scenarios, including microelectronics, microelectromechanical systems, solar cells, displays, etc. Inspired by the many advantages of PSPI, we have successfully prepared freestanding flexible films and transparent masks utilizing PSPI. This has simplified conventional shadow mask techniques while notably improving the resolution of the patterns. And we have successfully investigated and demonstrated the capability of PSPI flexible masks for the creation of arbitrary surface patterning, eliminating the need for pattern transfer and solvent usage. This advancement has the potential to facilitate future low-cost and large-scale production of integrated flexible electronic chips on a wide range of arbitrary surfaces.

2 | RESULTS AND DISCUSSION

2.1 | Fabrication of PSPI masks

Photolithography has been widely used for the processing of micro-nano devices due to its high-precision dimensions, exquisite structure, and rich functionality.^{41,42} To fabricate PSPI as masks, PSPI photoresist (PSPI-PR) was first coated onto a target substrate to form films and UV irradiation under rigid shadow masks to obtain the latent image of micropatterns. The preparation process of PSPI masks was carried out on different rigid substrates, that is, silicon dioxide/silicon (SiO_2/Si), quartz, and glass. Prior to the preparation process of PSPI mask, dust on the surfaces of SiO_2/Si substrate was removed with an air gun, while the surfaces of quartz and glass slides were pre-treated with an ultrasonic machine. The preparation of PSPI masks can be simplified into five main steps (Figure 1A). SiO_2/Si substrates were first treated with oxygen plasma, while a copper (Cu) layer with a thickness of tens of nanometers was first deposited on quartz or glass substrates. PSPI-PR was then spun on the rigid substrates. Desired micropatterns on PSPI films were fabricated through photolithography. PSPI films on rigid substrates were then subjected to a programmed heat treatment to form cured films via thermal imidization. The cured films were released from the substrates by placing the films and substrates in specific solutions. The films on SiO_2/Si substrates were immersed in a hydrofluoric acid (HF) solution for film stripping. On the other hand, the films on quartz or glass substrates were stripped off in a iron (III) chloride (FeCl_3) solution. The proposed release techniques were based on sacrificial layer removal, involving a mild reaction that results in the formation of the freestanding film masks without damaging the patterns (Figure S1a, b). Finally, the film masks were washed with deionized water to remove the solvent residue, and dried for the utilization in the next step (Figure 1B,C). The prepared freestanding flexible film was subsequently indicated as FFF.

The PSPI used is a negative photo-crosslinking photoresist, in which the photosensitive resin is cross-linked upon exposure to UV light to form a highly spatially structured polymer that is insoluble, accomplishing the conversion from soluble polyimide precursors to insoluble polyimides (Figure 1D). Photosensitive groups are introduced into the side chain of the polymer to create the soluble photoreactive polyimide precursor. When exposed to UV irradiation, the cross-linked systems of photosensitive groups are formed by free radical polymerization reactions that convert the soluble photoreactive polyimide precursor into an insoluble photo-crosslinked chemical intermediate.⁴³ The

photosensitive groups are cured at high temperatures and then removed to make patterned polyimide films.

2.2 | Physical characterization of FFF

Given that the bending stiffness of a film decreases with decreasing thickness, a thin film applied over arbitrary surfaces more closely follows the shape profile of the substrate underneath it than a thick film.⁴⁴ We successfully fabricated freestanding FFF with different thicknesses, as demonstrated by a scanning electron microscope (SEM) (Figure 2A). A confocal laser scanning microscope (CLSM) further showed the microscopic skeletonized structure of the FFF (Figure 2B) with a thickness of approximately 10 μm (Figure 2C). All FFF appeared as planar and smooth films. To optimize the fabrication of FFF, we further examined the effect of spin-coating speed on the thickness of FFF, showing a linear trend between speed and film thickness (Figure 2D). Following this conclusion, PSPI films of different thicknesses (5–20 μm) were fabricated for comparison (Figure 2E).

The light transmittance of FFF can vary with film thickness. Therefore, we measured the transmittance of the FFF films with different thicknesses. It is worth noting that we chose PSPI film for the transmittance experiments. The reason is that the skeletonized structure in the FFF would lead to higher transmittance due to the extra transmitting light through its patterned areas. In contrast, PSPI film ensures a relatively more precise assessment of the optical transmittance. The results showed an increased light transmittance with decreased film thickness of PSPI films (Figure 2F). The films exhibited outstanding optical transparency in the visible light band (380–780 nm). The thinnest PSP film (5 μm) had the highest light transmittance (>96%) and the thickest film of 20 μm had a transmittance of more than 86% (Table 1). As such, FFF would generally have high transparency, which is highly advantageous for the alignment of microelectrode patterns on the targeting material in the production of micro- and nano-devices. The high transparency of FFF would save the processing time of electronic devices and improve the success rate of device fabrication.

We then used a tensile tester to characterize the mechanical properties of PSPI films of various thicknesses, in order to verify the potential use of micropatterned FFF films as low-cost, reusable masks. As the thickness of the film increases, the maximum load (the force at failure) applied to the film specimen before fracture occurs proportionally (Figure 2G). The tensile properties of the films were calculated from the resulting force versus

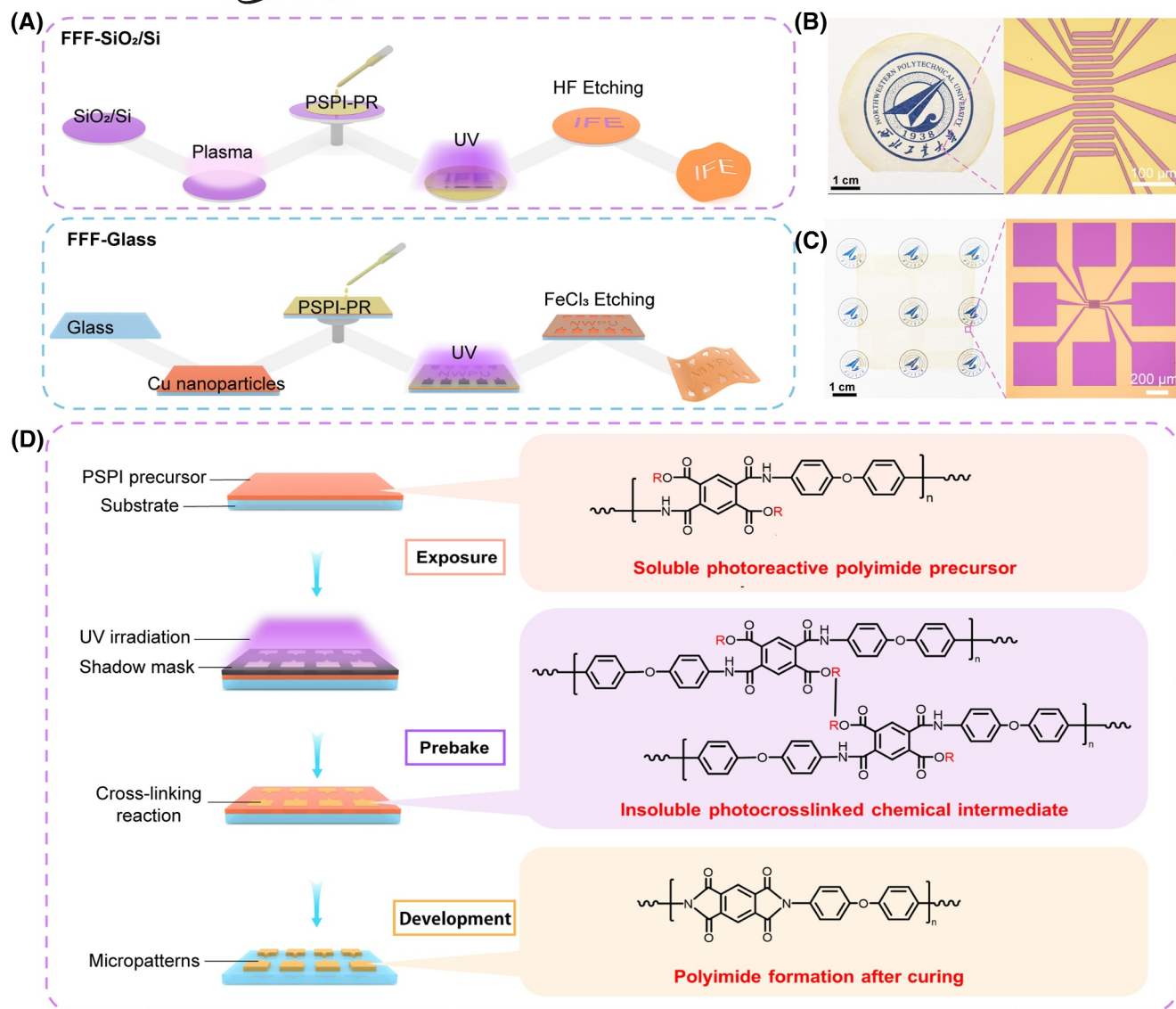


FIGURE 1 Fabrication of flexible and transparent masks. (A) Fabrication process of FFF by photolithography. (B) Photograph and magnified detail of a FFF prepared and released on SiO₂/Si substrate. (C) Photograph and magnified detail of a FFF prepared and released on glass substrate. (D) The PSPIs' photolithographic patterning procedures and photochemical reaction.

displacement curves. Tensile strength was calculated by dividing the force by the cross-sectional area of the film (thickness × width), and the elongation at break was determined by dividing the film displacement by the initial measured length⁴⁵ (Figure 2H). Detailed calculation processes can be found in Table S1. It can be observed that the films exhibit excellent tensile strength. We observed the normally distributed relationship between film thickness and tensile strength as well as between film thickness and elongation at break. The tensile strength and tensile strain of the 10 μm film simultaneously reached a maximum of 200 MPa and 54%, respectively. Young's modulus was determined to be the slope of the best-fit line in a plot of the axial stress versus strain.¹² We calculated the Young's modulus of the film

to be 3.5 ± 0.2 GPa. Comparatively, the Young's modulus of PDMS and parylene were reported to be 0.75–4 MPa⁴⁶ and 3.2 GPa,⁴⁷ respectively, and the Young's modulus of SU-8 was reported to be 2.2 ± 0.1 GPa.⁴⁸ The results of these comparisons show that FFF typically has a high Young's modulus, indicating that it has the potential to be used repeatedly without damage.

The process of micropatterning generally requires the use of physical vapor deposition methods (e.g., vacuum deposition, sputtering, etc.) or printing. To assess the heat stability of FFF during processing or use, we determined the glass transition temperature (*T_g*) of FFF by dynamic mechanical analysis (DMA). The curing process is critical for polyimide-based materials. This is because curing temperature affects the degree of molecular cross-linking,

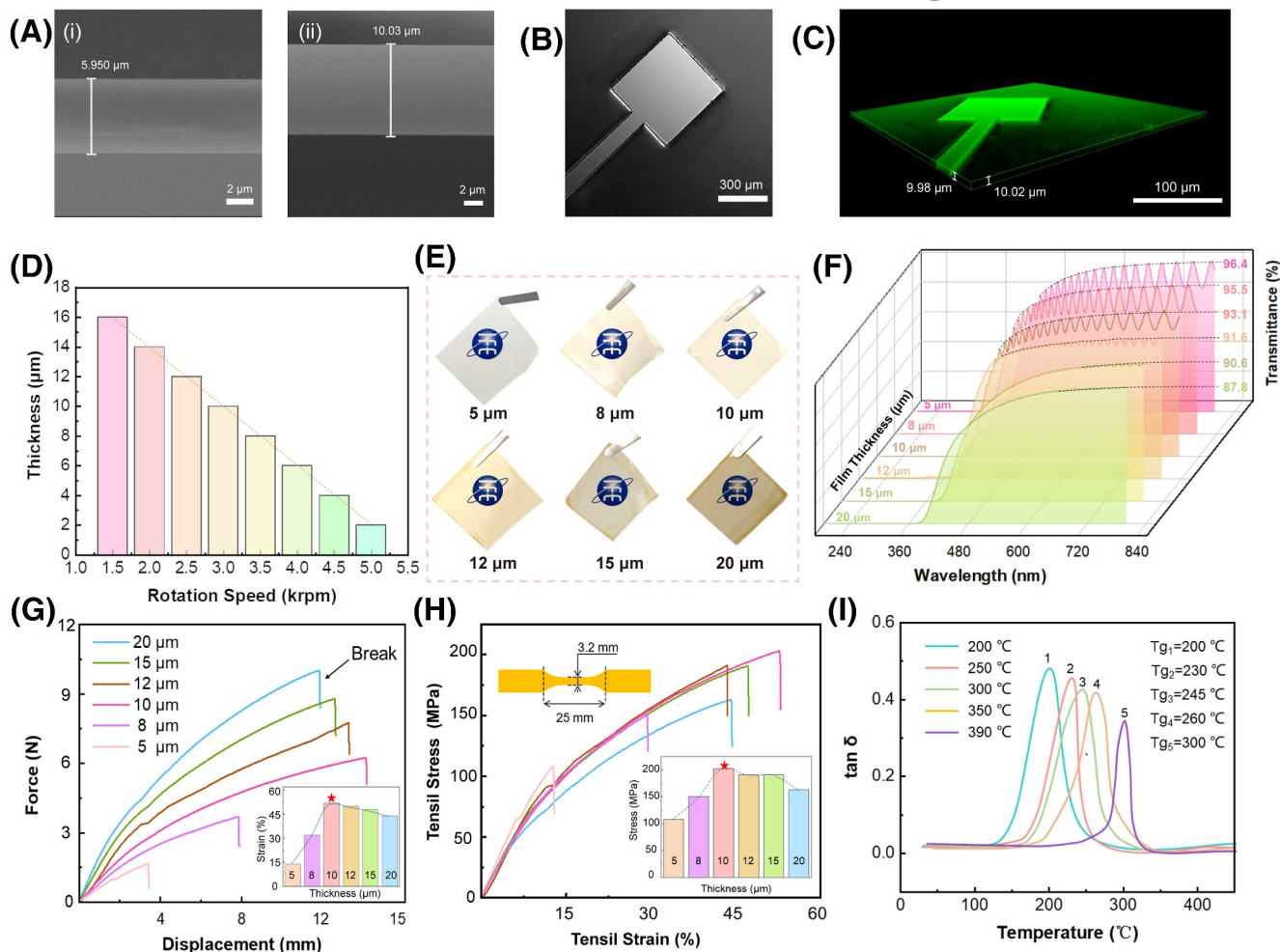


FIGURE 2 Characterization of the fabricated FFF. (A) scanning electron microscope images of cross-sections of films with thicknesses of approximately 6 μm (i) and 10 μm (ii). (B) CLSM image of a FFF film. (C) Slice-scanning CLSM image of a FFF film (Average thickness of 10 μm). (D) Effect of rotational speed for spin coating on the film thickness of FFF. (E) Photographs of films with thicknesses of 5 μm, 8 μm, 10 μm, 12 μm, 15 μm, and 20 μm. (F) Transmittance of films of different thickness. (G) Force-displacement curves for films of different thicknesses. (H) Stress-strain curves for films of different thicknesses. (I) dynamic mechanical analysis of FFF with different curing temperatures, mechanical loss factor ($\tan\delta$) of FFF over a range of temperature (T). CLSM, confocal laser scanning microscope.

TABLE 1 Optical properties of FFF with different film thickness, including the cut-off wavelengths (λ_0), transmittance at 500 nm ($T_{500\text{ nm}}$), transmittance at 700 nm ($T_{700\text{ nm}}$), and the maximum transmittance (T_{max}).

FFF thickness (μm)	λ_0 (%)	$T_{500\text{ nm}}$ (%)	$T_{700\text{ nm}}$ (%)	T_{max} (%)
5	374.0	75.8	87.1	96.4
8	351.0	77.5	83.8	95.5
10	351.5	77.5	91.7	93.1
12	379.5	81.4	89.7	91.6
15	372.0	67.1	86.9	90.6
20	360.5	68.0	86.2	87.8

which in turn affects T_g of the material.⁴⁹ Our FFF formation process had a wide range of curing temperatures (200–390°C). We measured T_g of the FFF formed at different curing temperatures (Figure 2I). It can be seen

that the T_g of FFF is as high as 300°C. FFF can be processed at higher temperatures compared to materials commonly used for flexible masks such as PDMS,⁵⁰ SU-8, and parylene-C, especially when the T_g of parylene-C is

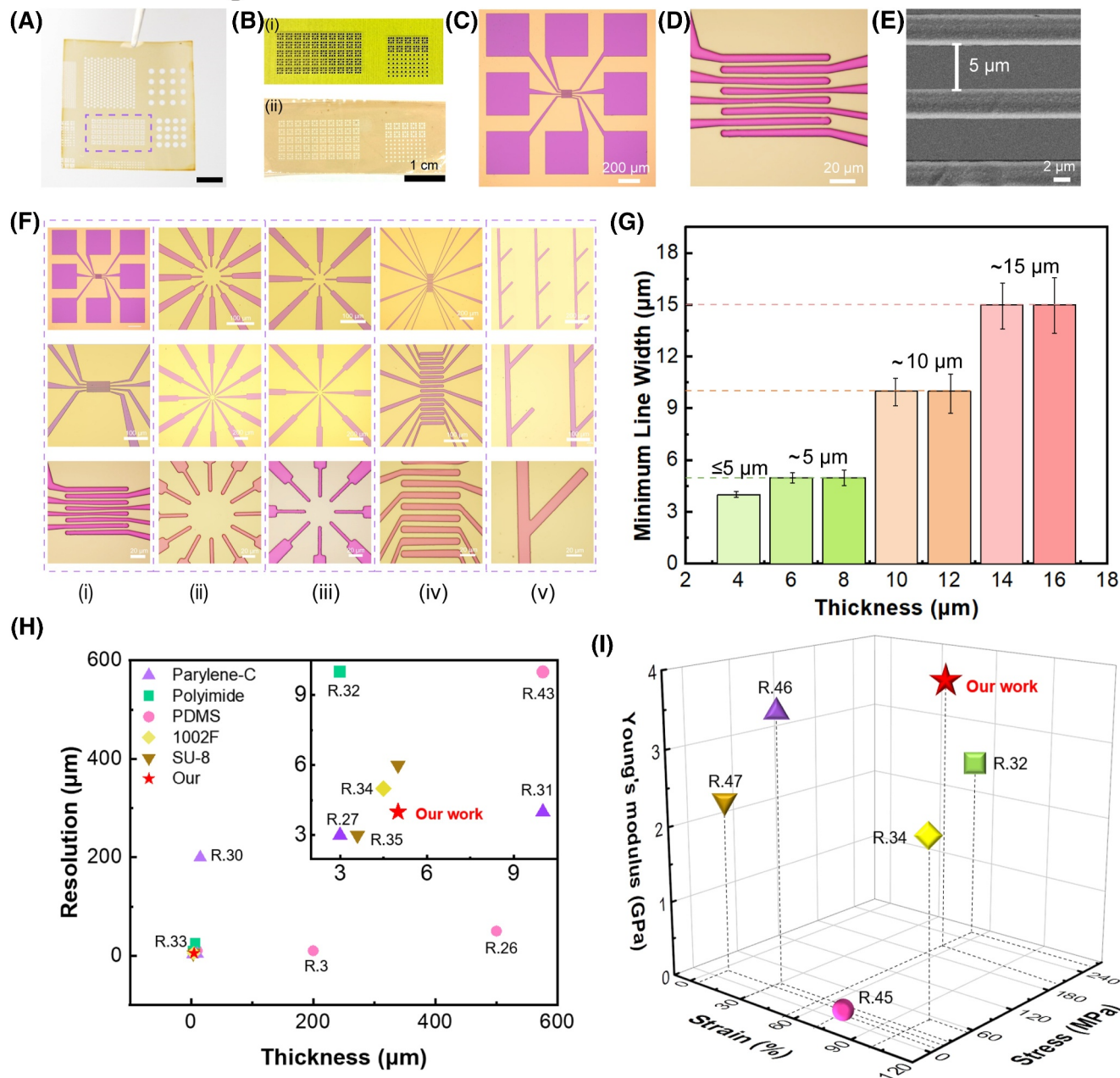


FIGURE 3 Characterization of the fabricated FFF. (A) Photograph of a FFF. (B) Magnified view of the photographs of the dashed box area with its corresponding rigid mask (i) and film (ii). (C) Optical micrograph of (B). (D) Optical micrograph of (C). (E) Scanning electron microscope micrograph of (D). (F) Optical micrographs of line widths of $5\ \mu\text{m}$ (i), $10\ \mu\text{m}$ (ii, iii), $15\ \mu\text{m}$ (iv), and $20\ \mu\text{m}$ (v). (G) Effect of film thickness of FFF on the maximum resolution (denoted by thinnest line width). (H) Comparison of the resolution of the prepared FFF with those reported in other studies. (I) Comparison of tensile strength, strain and Young's modulus of the prepared FFF with other materials used for the mask.

even less than 90°C .⁵¹ As a result, FFF can withstand high temperatures and exhibit unique advantages suitable for processing or usage in harsh circumstances.

To investigate the pattern resolution of FFF, we fabricated FFF with various patterns, line widths, and dimensions (Figure 3A and Figure S2). The patterns in a specific area of selected FFF film were transferred intact from a rigid chrome mask (Figure 3B). Optical

micrographs demonstrated that the progressively magnified electrode pattern was detailed (Figure 3C,D). SEM further demonstrated that the FFF successfully achieves a pattern size of $5\ \mu\text{m}$ (Figure 3E). In photolithography, given that in a condition with a fixed light energy, variation in film thickness of masks would affect their respective resolution. As such, we investigated the effect of the film thickness of FFF on their respective

resolution. Based on the recommendation from the manufacturer's material data sheet, PSPI-PR's optimum UV exposure energy is around 200 mJ cm^{-2} . With that, we set 200 mJ cm^{-2} as the fixed exposure energy and stick to it in this investigation, we prepared FFF with line widths of $5 \mu\text{m}$, $10 \mu\text{m}$, $15 \mu\text{m}$, and $20 \mu\text{m}$, we prepared FFF with line widths of $5 \mu\text{m}$, $10 \mu\text{m}$, $15 \mu\text{m}$, and $20 \mu\text{m}$. Optical micrographs showed that the shape of the patterns in FFF remained intact, demonstrating that the mask possesses high adaptability to different patterns (Figure 3F). Meanwhile, the maximum resolution gradually increases as the film thickness decreases (Figure 3G). For film thicknesses less than $8 \mu\text{m}$, a minimum line width of approximately $5 \mu\text{m}$ can be achieved, and for film thicknesses less than $5 \mu\text{m}$, the minimum line width will be less than $5 \mu\text{m}$. We also observe that thinner PSPI films yielded higher resolutions with minimal fluctuations in the resultant line width. In contrast, there are lower resolutions for the thicker PSPI films. It suggests that the thickness of the PSPI film affects the exposure process and the resultant pattern precision.

As a benchmark, we compared the resolution of FFF with other masks related work (Figure 3H and Table 2), and FFF can have high resolution when keeping the film freestanding. In addition, we compared the mechanical properties of FFF with different mask materials (Figure 3I and Table 2). It can be seen that the Young's modulus of the PSPI is much higher than other film materials, and the tensile strength is also higher than others, second only to PI. Meanwhile, the mechanical properties of PSPI exhibit significant superiority, which lays the foundation for the preparation of strong, unbreakable and reusable FFF.

2.3 | FFF for micropatterning on planar and nonplanar surfaces

We had successfully demonstrated the application of FFF for micropatterning on planar and nonplanar surfaces (Figure 4). The FFF was first placed delicately on the substrate and then thermally evaporated. Finally, FFF was removed to obtain substrates with diverse micropatterns. The keys to successful micropatterning processes are the precise positioning of the FFF on the substrate prior to thermal evaporation and the subsequent effective removal of FFF from the substrate. As the gap between the mask and the substrate has a direct impact on feature transfer fidelity, the mask should be kept in close contact with the substrate to reduce dimension distortion. The peeling process should also be scrutinized to ensure the

integrity and accuracy of the fabricated micropatterns. We demonstrated the use of FFF in micropatterning on arbitrary (both planar and nonplanar) surfaces, that is, Si substrate grown on two-dimensional material and leaves (Figure 4 and Figure S3). These results suggest that FFF can be widely used for micropatterning on different arbitrary surfaces.

Conventionally, to produce micropatterns on nonplanar surfaces, masks would first be adhered delicately to planar surfaces and bent to the shape of interest after micropatterning. We regard the conventional approach of producing micropatterns on nonplanar surfaces as indirect micropatterning. To validate the viability of FFF in micropatterning on nonplanar surfaces using indirect micropatterning, we first prepared a rectangular FFF measured at 5 mm length and $200 \mu\text{m}$ width (Figure S2d). The FFF were then placed on planar polyethylene terephthalate (PET) films, and a layer of gold (Au, 50 nm) was deposited on them to form micropatterns. The planar PET films were then bent into different radii of curvature (Figure 5A). The bending of PET films was controlled by a stepper motor, and the stepping distance required for different radii was calculated using Equation (1).⁵²

$$C = 2r \sin(L/2r) \quad (1)$$

In the above equation, L is the length of PET film, r is predetermined, and C is the base length used to produce curvatures of interest (stepping distance of the stepper motor).

The current-voltage characteristic experiment demonstrated that nonplanar microelectrodes fabricated with indirect micropatterning with a curvature radius of 60 mm or less were not able to conduct electricity (Figure 5B). Optical contrast micrographs of a microelectrode with a curvature radius of 60 mm fabricated with indirect micropatterning in light and dark fields showed that there were many cracks within it, inhibiting it from conducting electricity (Figure 5C,D). Nonplanar microelectrodes with a curvature radius of 80 and 100 mm were able to conduct electricity, but in an unsatisfactory manner, in which their current-voltage characteristic deviated from the baseline—the current-voltage characteristic of planar microelectrode (control). We further derived the corresponding bending strains (ε) for each radius of curvature from Equation (2)⁵³ and calculated the resistance of the respective microelectrodes from Ohm's law (Table 3 and Table S2).

$$\varepsilon = \frac{Z}{2r} \quad (2)$$

TABLE 2 Comparison of the physical properties of the prepared FFF with those reported in other studies.

Material	Thickness (μm)	Resolution (μm)	Strain	Stress	Young's modulus	Reference
PDMS	200	10	-	-	-	3
PDMS	100	40	78%	140 kPa	0.75–4 MPa	23
PDMS	20	250	-	-	-	24
PDMS	500	50	-	-	-	26
PDMS	10	10	-	-	-	44
SU-8-PDMS	250	500	-	-	-	25
SU-8	3.6	3	-	-	-	35
SU-8	5	6	-	-	-	36
SU-8	-	-	$1.2 \pm 0.5\%$	22 ± 7 MPa	2.2 ± 0.1 GPa	48
Parylene-C	15	200	-	-	-	30
Parylene-C	10	4	-	-	-	31
Parylene-C	-	-	-	34.5 MPa	3.2 GPa	47
Parylene-C	3	3	-	-	-	37
Polyimide	3	10	50%	250 MPa	2.23 GPa	32
Polyimide	7.5	25	-	-	-	33
1002F	4.5	5	$105.1 \pm 0.5\%$	54.5 ± 3.1 MPa	1.43 ± 0.20 GPa	34
Stainless steel-aluminum thin films	200	200	-	-	-	19
Our work	5	About 5	50%	200 MPa	3.5 ± 0.2 GPa	-

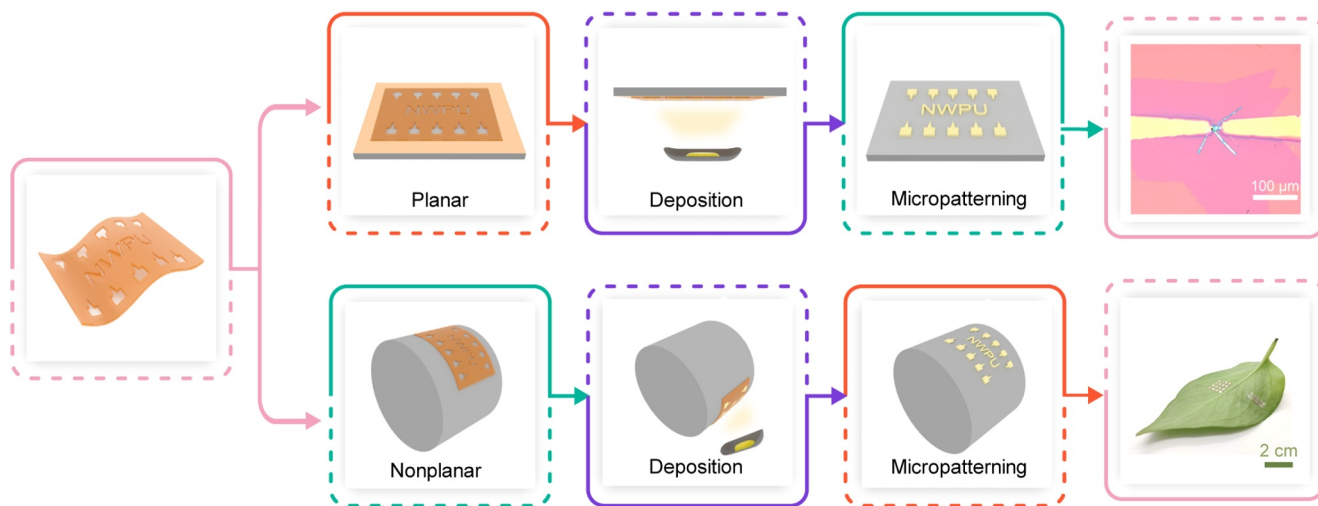


FIGURE 4 Micropatterning process using freestanding flexible masks.

In the above equation, ε is the bending strain of the microelectrode, Z is the thickness of the substrate (in this case was PET film, 200 μm), and r is the radius of curvature.

We envisioned that preparing electrode patterns directly on the targeting nonplanar substrate would

prevent devices from electrode breakage associated with the bending of electrodes during the transferring process from planar surfaces to nonplanar shapes. To test the hypothesis, we affixed six FFF with the same dimensions to nonplanar substrates with different radii of curvature and performed vapor deposition of Au (50 nm) directly

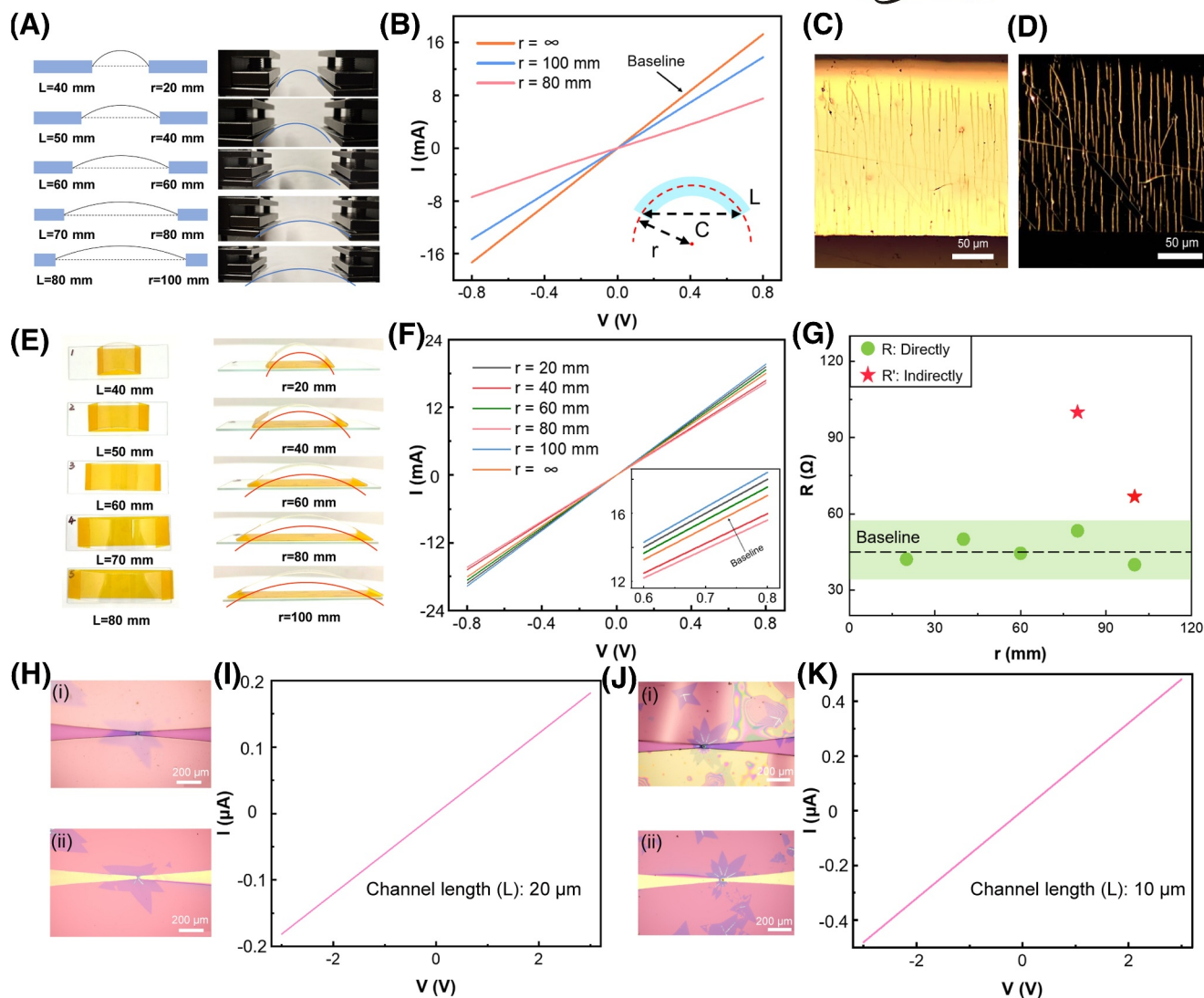


FIGURE 5 Comparison of direct and indirect preparation of electrodes. (A) Schematic illustrations and photographs of polyethylene terephthalate substrates with the same electrode pattern being bent to different radii of curvature. (B) Current-voltage characteristic for electrodes bent to different radii of curvature on a curved surface. (C) Optical micrograph of the light field of a bent electrode producing many cracks and (D) the corresponding dark field photograph. (E) Schematic illustrations and photographs of curved surfaces with different radius of curvatures were simulated using PI tapes and PET films. (F) Current-voltage characteristic for electrodes on curved surfaces with different radius of curvatures. (G) Resistance of electrodes with different radius of curvatures (R and R' are denoted by direct and indirect micropatterning process, respectively). (H) Optical micrograph of the photosensitive polyimide mask aligned with a counter electrode pattern with a channel length of $20\ \mu\text{m}$ (i) and direct metal deposition (ii). (I) Current-voltage characteristic for a device with a channel length of $20\ \mu\text{m}$. (J) Optical micrograph of the mask aligned with a counter electrode pattern with a channel length of $10\ \mu\text{m}$ (i) and direct metal deposition (ii). (K) Current-voltage characteristic for a device with a channel length of $10\ \mu\text{m}$.

on them to form micropatterns. We regard this approach as direct micropatterning. Nonplanar surfaces with different radii of curvatures were simulated using polyimide (PI) tapes and PET films with a thickness of $200\ \mu\text{m}$ (Figure 5E). PET films with different lengths and their respective predetermined radius of curvatures were used to derive the corresponding base lengths for producing curvatures of interest using Equation (1) (Figure 5F), where C was the length of the PI tapes. The current-voltage characteristic curve showed that all

nonplanar microelectrodes fabricated with direct micropatterning were able to conduct electricity. There was no significant difference in the electrical behaviors of microelectrodes with different radii of curvature and planar microelectrodes (control) (Figure 5F). We derived the resistance of the respective microelectrodes from Ohm's law (Table 4). Detailed calculation processes can be found in Table S3.

To learn about the electrical behavior of microelectrodes produced from indirect and direct micropatterning

TABLE 3 Parameters of bending to different radii of curvature for the electrode, including compression length (ΔL), bending strain (ϵ), and resistance.

L (mm)	r (mm)	C (mm)	Compressive lengths (ΔL) (mm)	Bending strain (ϵ)	Resistance (Ω)
40	20	33.66	6.34	5.00×10^{-3}	-
50	40	46.80	3.20	2.50×10^{-3}	-
60	60	57.53	2.47	1.67×10^{-3}	-
70	80	67.79	2.21	1.25×10^{-3}	100.0
80	100	77.88	2.12	1.00×10^{-3}	66.7

Note: The compression length is given in millimeters (mm), while the bending strain and resistance are dimensionless and are defined as the ratio of the change in length of the electrode due to bending to its original length. Resistance is measured in Ohms (Ω) and is normalized to the resistance of the electrode at a radius of curvature of infinity (planar).

TABLE 4 Resistance of electrodes with different radii of curvature.

r (mm)	L (mm)	C (mm)	Resistance (Ω)
∞	-	-	47.1
20	40	33.66	42.1
40	50	46.80	50.0
60	60	57.53	44.4
80	70	67.79	53.3
100	80	77.88	40.0

Note: Data are shown as the mean \pm standard deviation of n repetitions, where the resistance of the electrode with an infinite (planar) radius of curvature is used as the baseline.

processes, we overlaid resistances of microelectrodes with different radii of curvature in a plot (Figure 5G). The resistances of microelectrodes made by the conventional indirect micropatterning process (R') with a radius of 80 mm or 100 mm had a large deviation from the baseline. In contrast, a small deviation in the resistance (R) is observed for the directly patterned microelectrodes. We deduced that direct micropatterning preparation on nonplanar substrate would prevent devices from electrode breakage associated with the bending of electrodes during the transferring process from planar surfaces to nonplanar shapes. These results provide important insights into the preparation of microelectrodes on nonplanar surfaces and suggest that an in situ micropatterning processes on nonplanar surfaces would have a greater success rate in fabricating microelectrodes.

2.4 | FFF for micropatterning of electronic devices

Micro- and nano-scale devices are typically fabricated by photolithography and wet etching procedures, in which numerous chemical solvents are usually required for

developing micropatterns and washing. Some chemical solvents may react with materials utilized for electronic processing, and eventually affect the performance of electronic devices. To overcome the aforementioned problem, electrodes can be formed directly using masks to fabricate electronic devices. To prove the capability of FFF in the low-dimensional material micropatterning process (i.e., molybdenum disulfide, MoS_2), we fabricated FFF with counter electrode patterns. The high transparency of FFF allows easy and precise alignment on the low-dimensional semiconductor materials (Figure 5H-i and J-i). The masks with counter-electrode patterns were aligned with MoS_2 (pre-grown on silicon wafers via CVD) and deposited with Au (Figure 5H-ii and J-ii). The fabrication of microelectronic devices with the help of FFF was successful. There was no mechanical disruption or tearing of films during these experiments. High-resolution micropatterns (10 and 20 μm) were able to be fabricated with FFF, implying that FFF is suited for high-resolution electronic applications. We further tested the functionality of the electronic devices. The current-voltage characteristic analysis showed that both could conduct electricity, with a channel gap of 10 μm possessing better conductivity than a channel gap of 20 μm (Figure 5I,K). This has proven the workability of FFF as an efficient shadow mask for micropatterning in high-resolution electronic applications. With FFF, the processing and manufacturing of electronics can be simplified. More appealingly, the incorporation of FFF could reduce the processing time while increasing the success rate of electronic manufacturing.

3 | CONCLUSIONS

In this study, we present a versatile and efficient micropatterning technique by taking advantage of as-fabricated PSPI masks. A high-performance mask can be attached to arbitrary surfaces and has a high degree of pattern

flexibility. Additionally, the masks are available in a wide range of shapes and dimensions to suit diverse requirements. By eliminating the need for pattern transfer processes and the use of solvents, this technology overcomes the limitations of conventional patterning methods and enables direct micropatterning on non-planar surfaces. The characterization and results of PSPI masks in terms of thickness (5–20 μm), resolution (sub-5 μm), transparency (>96%), temperature resistance (300°C), and mechanical performance (3.5 GPa) reveal the great potential for micropatterning. The versatility of the PSPI mask was further demonstrated by successfully forming micropatterns directly on various substrates, including rigid SiO_2/Si wafers, flexible PET films, and intricate leaf surfaces. This successful application highlights the effectiveness of PSPI masks in creating precise micropatterns on a wide range of arbitrary surfaces. The utilization of fabricated PSPI masks can minimize performance degradation introduced by traditional electronics processes, reduce manufacturing cycle time and cost, and enhance the success rate of producing advanced flexible electronic chips.

4 | EXPERIMENTAL SECTION

4.1 | Materials

All chemicals were obtained from commercial sources and used without further purification. PSPI negative photoresist PIMEL BL-301 (PSPI-PR), developer A-515, and corresponding rinse agent C-260 were purchased from Asahi Kasei Co., Ltd. (Japan). Hydrofluoric acid solution (AR, 40%) was purchased from RHAWN (Shanghai, China). Iron (III) chloride (FeCl_3) power ($\geq 99.99\%$ based on trace metals analysis) was purchased from Sigma-Aldrich. Deionized water was prepared by the Millipore NanoPure purification system (resistivity higher than 18.2 $\text{M}\Omega\text{ cm}^{-1}$).

4.2 | Preparation of PSPI masks (FFF) on SiO_2/Si substrates

Plasma treatment was performed on SiO_2/Si substrates to enhance their surface hydrophilicity (Atmospheric Plasma Cleaner JL-V02, Shenzhen City JinLai Technology Co., Ltd., China). A layer of PSPI-PR was spin-coated onto SiO_2/Si substrates with three sequential speeds (spin coater: KW-4C, Beijing SEDERSKAY Electronics Co., China). The spin coater's parameters used were 1000 rpm–10 s, 3000 rpm–60 s, and 1500 rpm–15 s. SiO_2/Si substrate was baked at 100°C for 240 s (heating plate: C-

MAG HP10 IKA, Germany). Microelectrode patterns were transferred from the rigid shadow mask to the SiO_2/Si substrate via UV irradiation at 200 mW cm^{-2} (URE-2000/35, Institute of Optoelectronics Technology, Chinese Academy of Sciences, China). By measuring the UV intensity with an UV radiometer, we can determine the required exposure time by dividing the exposure energy of 200 mW cm^{-2} by the measured UV intensity. The SiO_2/Si substrate was left to develop with A-515 for 22 s and rinsed with C-260 for 5 s. The surface was blown-dry with an air gun and placed either on a hot plate at 45°C for 120 s or at room temperature for 20 min. The SiO_2/Si substrate was then put into the oven (DHG-9055AD, Shanghai Qixin Scientific Instruments Co., China) to be cured into a film. The heating sequence parameter was as follows: 30°C \rightarrow 100°C \rightarrow 150°C \rightarrow 200°C \rightarrow 150°C \rightarrow 100°C \rightarrow 30°C (each heating cycle took 10 min and was held for 30 min). The SiO_2/Si substrate containing the mask was immersed in a hydrofluoric acid solution with a mass fraction of about 40% for 10–30 min. The masks can then be released from the substrate. Finally, the film was washed with deionized water. Excess water was removed from the surface of the film through blot drying, air gun, or a vacuum oven.

4.3 | Preparation of PSPI masks (FFF) on glass substrates

The glass surface was cleaned in an ultrasonic bath (KQ-50DE, Kunshan Ultrasonic Instruments Co., China) with acetone for 3 min and subsequently with deionized water for 1 min. Cu (100 nm) was then deposited on the glass surface by the thermal evaporation system (VZZ-400, VNANO, China). The subsequent preparation steps of FFF on glass substrate were the same as the aforementioned preparation of FFF on SiO_2/Si substrate—spin coating, photolithography, and curing. The mask was then released from the glass substrate in FeCl_3 solution with a mass fraction of $\geq 30\%$ for 10–30 min. Finally, the film was washed and dried using the same method of preparation of FFF on SiO_2/Si substrate.

4.4 | Characterization

Optical images of masks were obtained using a microscope (ZEISS Primotech, Germany). Brightfield images were acquired with white-light illumination. And using a camera that was sensitive to the scattered light to acquire darkfield images. Field Emission SEM images were performed by the Gemini SEM 300 (Germany) at an accelerating voltage of 5 kV. FFF were coated with gold using

a sputter coater to improve conductivity and reduce charging effects. Imaging was performed at a working distance of 5–10 mm with a beam current of 2–3 nA. CLSM images were acquired using a Leica TCS SP8 (Germany) CLSM equipped with a 63x oil-immersion objective and a 488 nm laser for excitation of GFP fluorescence. The mechanical properties of the film were measured using a double-column universal tester (United States, Instron 5569) according to ASTM D638-14. The film specimens were cut into dog bone shapes using a Type 5 mold. The specimens were then clamped between the grips of the universal tester and subjected to a tensile load at a constant crosshead speed of 10 mm/min, and the force-displacement curves were recorded automatically. The transmittances of films were measured by a UV-visible spectrophotometer (U-3310, Hitachi, Japan). Each PSPI film was placed on the sample holder of the spectrophotometer, and transmittance was measured over a range of wavelengths from 200 to 800 nm at room temperature. The spectrophotometer was calibrated using air as the reference, and the data was processed using software provided by the manufacturer. The glass transition temperature of PSPI film was measured by a dynamic mechanical analyzer (DMA 242E, NETZSCH, Germany) with a heating rate of 2 °C/min. The mechanical loss factor ($\tan \delta$) was plotted versus temperature (T) for PSPI film. The position of $\tan \delta$ at the peak was taken as the glass transition temperature of PSPI-PR.

4.5 | Micropatterning and electrical measurements

FFF were attached to the PET films and leaves. Au (50 nm) was deposited on the substrates by the thermal evaporation system (VZZ-400, VNANO, China). The aforementioned step was repeated for the preparation of an electrical device, where FFF was aligned and adhered to MoS₂ through an optical microscope. The electrical measurements were carried out in a probe station (Cindbest, CS-4, China) by a semiconductor parameter analyzer (PDA FS380 Pro, Platform Design Automation). A bias voltage from –3.0 to 3.0 V was applied between the Au electrodes to characterize the in-plane current-voltage properties. The stepper motor mentioned in the context was custom-built by the research group.

AUTHOR CONTRIBUTIONS

Xuan Dong: Data curation; formal analysis; investigation; methodology; writing – original draft; writing – review & editing. **Siew Yin Chan:** Project administration; supervision; writing – review & editing. **Ruoqing Zhao:** Data curation; methodology. **Lei Luo:** Software.

Manzhang Xu: Methodology; validation. **Jiuwei Gao:** Software; validation. **Xin Ju:** Methodology; writing – review & editing. **Jing Wu:** Validation. **Dongzhi Chi:** Supervision. **Xian Jun Loh:** Supervision. **Xuewen Wang:** Conceptualization; funding acquisition; project administration; supervision.

ACKNOWLEDGMENTS

The authors gratefully acknowledge financial support by the National Natural Science Foundation of China (62288102, 62304182, and 62371397), the Natural Science Foundation of Shaanxi Province (2022JQ-659 and 2023-JC-YB-495), and the Fundamental Research Funds for the Central Universities, the start-up funds from Northwestern Polytechnical University (23GH02028). X. J., J. W. and D. C. acknowledge the National Research Foundation Competitive Research Program (NRFCRP24-2020-0002).

CONFLICT OF INTEREST STATEMENT

Xian Jun Loh is an editorial board member of this journal and was not involved in the editorial review or the decision to publish this article. The authors declare no conflict of interests.

DATA AVAILABILITY STATEMENT

The data that support the findings of this study are available from the corresponding author upon reasonable request.

ORCID

Xuewen Wang  <https://orcid.org/0000-0002-9689-6678>

REFERENCES

1. J. del Barrio, C. Sánchez-Somolinos, *Adv. Opt. Mater.* **2019**, 7(16), 1900598.
2. G. Zabow, *Science* **2022**, 378, 894.
3. J. Yin, S. Wang, A. Di Carlo, A. Chang, X. Wan, J. Xu, X. Xiao, J. Chen, *Med-X.* **2023**, 1, 3.
4. A. Libanori, G. Chen, X. Zhao, Y. Zhou, J. Chen, *Nat. Electron.* **2022**, 5, 142.
5. X. Zhao, Y. Zhou, J. Xu, G. Chen, Y. Fang, T. Tat, X. Xiao, Y. Song, S. Li, J. Chen, *Nat. Commun.* **2021**, 12(1), 6755.
6. G. Chen, X. Xiao, X. Zhao, T. Tat, M. Bick, J. Chen, *Chem. Rev.* **2021**, 122, 3259.
7. Y. Zhou, X. Zhao, J. Xu, Y. Fang, G. Chen, Y. Song, S. Li, J. Chen, *Nat. Mater.* **2021**, 20, 1670.
8. J. Yin, S. Wang, T. Tat, J. Chen, *Nat. Rev. Bioeng.* **2024**, 1.
9. H. Li, Z. Wang, Y. Cao, Y. Chen, X. Feng, *ACS Appl. Mater. Interfaces.* **2020**, 13, 1612.
10. Y. Yoshida, H. Wada, K. Izumi, S. Tokito, *Jpn J. Appl. Phys.* **2017**, 56, 05EA01.
11. J. J. Adams, E. B. Duoss, T. F. Malkowski, M. J. Motala, B. Y. Ahn, R. G. Nuzzo, J. T. Bernhard, J. A. Lewis, *Adv. Mater.* **2011**, 23, 1335.

12. Q. Wang, M. Tahir, J. Zang, X. Zhao, *Adv. Mater.* **2012**, *24*, 1947.
13. K. E. Paul, M. Prentiss, G. M. Whitesides, *Adv. Funct. Mater.* **2003**, *13*, 259.
14. L. Wong, J. D. Pegan, B. Gabela-Zuniga, M. Khine, K. E. McCloskey, *Biofabrication* **2017**, *9*, 021001.
15. H. G. Craighead, *Science* **2000**, *290*, 1532.
16. M. M. H. Shandhi, M. Leber, A. L. Hogan, D. J. Warren, R. Bhandari, S. Negi, *Off. Syst.* **2017**, *26*, 376.
17. W. Shang, G. Q. Gu, F. Yang, L. Zhao, G. Cheng, Z.-l. Du, Z. L. Wang *ACS Nano*. **2017**, *11*, 8796.
18. I.-Y. Chung, J.-D. Kim, K.-H. Kang, *Int. J. Precis Eng. Manuf.* **2009**, *10*, 11.
19. H. Gnanasambanthan, D. Maji, *IEEE 7th International Conference for Convergence in Technology (I2CT)*, IEEE **2022**.
20. W. J. Hyun, E. B. Secor, M. C. Hersam, C. D. Frisbie, L. F. Francis, *Adv. Mater.* **2015**, *27*, 109.
21. S. Xie, V. Savu, W. Tang, O. Vazquez-Mena, K. Sidler, H. Zhang, J. Brugger, *Microelectron Eng.* **2011**, *88*, 2790.
22. K. Sidler, L. G. Villanueva, O. Vazquez-Mena, V. Savu, J. Brugger, *Nanoscale* **2012**, *4*, 773.
23. A. Folch, B. H. Jo, O. Hurtado, D. J. Beebe, M. Toner, *J. Biomed. Mater. Res.* **2000**, *52*, 346.
24. P. Jothimuthu, A. Carroll, A. A. S. Bhagat, G. Lin, J. E. Mark, I. Papautsky, *J. Micromech. Microeng.* **2009**, *19*(4), 045024.
25. J. H. Choi, H. Lee, H. K. Jin, J.-S. Bae, G. M. Kim, *Lab Chip* **2012**, *12*, 5045.
26. J. H. Choi, G. M. Kim, *Int. J. Precis Eng. Manuf.* **2011**, *12*, 165.
27. J. N. Lee, X. Jiang, D. Ryan, G. M. Whitesides, *Langmuir* **2004**, *20*, 11684.
28. T. Wang, Y. Xi, M. Hu, B. Yang, W. Liu, J. Liu, *Off. Syst.* **2018**, *27*, 698.
29. D. Lee, S. Yang, *ACS Appl. Mater. Interfaces.* **2013**, *5*, 2658.
30. S. Jinno, H. C. Moeller, C. L. Chen, B. Rajalingam, B. G. Chung, M. R. Dokmeci, A. Khademhosseini, *J. Biomed. Mater. Res., Part A* **2008**, *86*, 278.
31. S. Selvarasah, S. Chao, C.-L. Chen, S. Sridhar, A. Busnaina, A. Khademhosseini, M. Dokmeci, *Sens. Actuators, A A.* **2008**, *145*, 306.
32. D. Martinez, C. Py, M. Denhoff, R. Monette, T. Comas, A. Krantis, G. Mealing, *Biotechnol. Bioeng.* **2013**, *110*, 2236.
33. Y. Kajiyama, K. Joseph, K. Kajiyama, S. Kudo, H. Aziz, *Appl. Phys. Lett.* **2014**, *104*, 26.
34. D. Ornoff, Y. Wang, N. Allbritton, *J. Micromech. Microeng.* **2012**, *23*, 025009.
35. J. Choi, A. Roychowdhury, N. Kim, D. E. Nikitopoulos, W. Lee, H. Han, S. Park, *J. Micromech. Microeng.* **2010**, *20*, 085011.
36. G. Kim, B. Kim, J. Brugger, *Sens. Actuators, A* **2003**, *107*, 132.136.
37. T. Wang, M. Hu, B. Yang, X. Wang, J.-Q. Liu, *IEEE Micro Electro Mechanical Systems (MEMS)*, IEEE **2018**.
38. Y. S. Negi, S. R. Damkale, S. Ansari, *J. Macromol. Sci., Polym. Rev.* **2001**, *41*, 119.
39. M. Yoshida, T. Hirata, M. Fujita, N. Anzai, N. Tamura, J. Photopolym, *Sci. Technol.* **2014**, *27*, 207.
40. M. Tomikawa, R. Okuda, H. Ohnishi, J. Photopolym, *Sci. Technol.* **2015**, *28*, 73.
41. D.-H. Kim, N. Lu, R. Ma, Y.-S. Kim, R.-H. Kim, S. Wang, J. Wu, S. M. Won, H. Tao, A. Islam, *Science* **2011**, *333*, 838.
42. L. Tian, Y. Li, R. C. Webb, S. Krishnan, Z. Bian, J. Song, X. Ning, K. Crawford, J. Kurniawan, A. Bonifas, *Adv. Funct. Mater.* **2017**, *27*, 1701282.
43. R. Rubner, A Photopolymer. The Direct Way to Polyimide Patterns **1979**.
44. H. Wang, A. Chakraborty, C. Luo, *J. Micromech. Microeng.* **2010**, *20*, 127001.
45. K. Masamba, Y. Li, J. Hategekimana, F. Liu, J. Ma, F. Zhong, *J. Food Sci. Technol.* **2016**, *53*, 2227.
46. D. Fuard, T. Tzvetkova-Chevolleau, S. Decossas, P. Tracqui, P. Schiavone, *Microelectron. Eng.* **2008**, *85*, 1289.
47. D. Wright, B. Rajalingam, J. M. Karp, S. Selvarasah, Y. Ling, J. Yeh, R. Langer, M. R. Dokmeci, A. Khademhosseini, *J. Biomed. Mater. Res., Part A* **2008**, *85*, 530.
48. J. Gao, L. Guan, J. Chu, *Sixth International Symposium on Precision Engineering Measurements and Instrumentation*, SPIE **2010**.
49. J. D. Russell, J. L. Kardos, *Polym. Compos.* **1997**, *18*, 595.
50. S. K. Mitra, S. Chakraborty, *Microfluidics and Nanofluidics Handbook: Fabrication, Implementation, and Applications*, Taylor and Francis **2012**.
51. H.-S. Noh, K.-S. Moon, A. Cannon, P. J. Hesketh, C. Wong, *J. Micromech. Microeng.* **2004**, *14*, 625.
52. X. Liao, Q. Liao, X. Yan, Q. Liang, H. Si, M. Li, H. Wu, S. Cao, Y. Zhang, *Adv. Funct. Mater.* **2015**, *25*, 2395.
53. F. Li, T. Shen, L. Xu, C. Hu, J. Qi, *Adv. Electron Mater.* **2019**, *5*, 1900803.

SUPPORTING INFORMATION

Additional supporting information can be found online in the Supporting Information section at the end of this article.

How to cite this article: X. Dong, S. Y. Chan, R. Zhao, L. Luo, M. Xu, J. Gao, X. Ju, J. Wu, D. Chi, X. J. Loh, X. Wang, *FlexMat* **2024**, *1*, 203. <https://doi.org/10.1002/flm2.18>